Equation of state and phase diagram of water at ultrahigh pressures as in planetary interiors

Martin French,[1] Thomas R. Mattsson,[2] Nadine Nettelmann,[1] and Ronald Redmer[1]

[1]*Institut für Physik, Universität Rostock, D-18051 Rostock, Germany*
[2]*Pulsed Power Sciences Center, Sandia National Laboratories, Albuquerque, New Mexico 87185-1186, USA*

We present QMD simulations of water in the ultra-high-pressure regime up to conditions typical for the deep interior of Jupiter and Saturn. We calculate the equation of state and the Hugoniot curve and study the structural properties via pair correlation functions and self-diffusion coefficients. In the ultradense superionic phase, we find a continuous transition in the protonic structure. With rising density, the mobile protons stay with increasing probability at the octahedral sites while leaving the ice X positions to the same degree unoccupied. Water forms a fluid dense plasma at the conditions of Jupiter's core (i.e., 20 000 K, 50 Mbar, 11 g/cm^3), while it may be superionic in the core of Saturn. We expect a substantial amount of superionic water inside Neptune.

I. INTRODUCTION

Water is not only one of the prevalent materials in nature but also a prime example for a material having a rich phase diagram with a variety of structural transitions.[1] Especially, quantum molecular dynamics (QMD) simulations predict the existence of a superionic phase in the high pressure regime at several megabars.[2] Here, we present QMD simulations of water in the ultra-high-pressure regime up to 100 Mbar (15 g/cm^3) and several thousand Kelvin. Of special interest is the identification and location of the phase transition between superionic water and dense water plasma. We find, within the superionic phase, a rearrangement in the hydrogen structure with increased density. The exotic superionic phase, described in detail by Cavazzoni *et al.*[2] and later by Goldman *et al.*,[3] is characterized by highly mobile protons diffusing through a solid bcc oxygen lattice. It is expected to have boundaries with high pressure ice phases for temperatures less than 2000 K[2,4,5] and supercritical fluid water which transforms to an electronically conductive dense plasma above 4000 K.[6] The knowledge of the behavior of water at high pressures has wide applications in astrophysics and shock physics. Water is known to be a major constituent of giant planets.[7,8] The cores of Jupiter and Saturn are believed to consist of a mixture of hot ices (mostly water but also methane and ammonia) and rocks.[9,10] Planetary models[11–15] predict different temperatures of about 16000–21000 K and pressures of 40–50 Mbar for the core of Jupiter; the respective numbers for Saturn are 8000–12000 K and 8–18 Mbar. It is also expected that Uranus and Neptune as well as some extrasolar planets contain major amounts of water in their envelopes along with comparable amounts of methane and ammonia.[7,8,16] Models of giant planets require accurate equations of state (EOS) data up to ultrahigh densities as input to produce realistic results which meet the observational constraints.[15] Thermodynamic conditions as occurring in the cores of Jupiter and Saturn have not been realized experimentally yet, so that *ab initio* calculations (see Ref. 17 for general information) as performed here are an important step forward to a better understanding of matter under such extreme conditions.

II. QUANTUM MOLECULAR DYNAMICS SIMULATIONS

We employ the Vienna *Ab Initio* Simulation Package (VASP 4.6)[18] for the QMD simulations. It includes electronic structure calculations based on finite temperature density-functional theory (DFT)[19–21] while regarding the ions as classical particles. We use the PBE (Ref. 22) exchange-correlation functional and projector augmented wave (PAW) pseudopotentials[23] for the electron-ion interactions in the DFT calculations. Extensive convergence tests, see Appendix A for details, are performed, e.g., with respect to the cutoff energy, the simulation time, particle number and **k** points yielding an accuracy of better than 2% in the EOS data. Especially, the proper function of the pseudopotentials has to be ensured since we perform simulations for ultradense systems. Within the range of our calculations (295–130000 K and 1−20 g/cm^3), we use the standard hydrogen (1 free electron per ion) and oxygen (6 free electrons per ion) potentials provided by VASP 4.6[18] with an energy cutoff of 900 eV and evaluate the electronic states at the Γ point. The highest temperatures as well as selected high-density points were investigated using an all-electron PAW core potential.[24] The all-electron PAW core potential requires an energy cutoff of 2000 eV and yields EOS results within 1.5% accuracy compared with the standard oxygen potential and the same structural properties as well. Most simulations are performed with 54 H$_2$O molecules in a canonical ensemble with the temperature T, volume V, and particle number N as independent variables. The ion temperature is controlled by a Nosé thermostat.[25] We calculate the thermal EOS $p(T,V,N)$, the caloric EOS $U(T,V,N)$, and the principal Hugoniot curve. We also obtain the self-diffusion coefficient of the ions by the mean square displacement method, see Appendix B for details. Furthermore, the radial ion-ion pair correlation functions are calculated to examine structural information. The location of the plasma-to-superionic phase transition is qualified by using an equilibrated superionic starting ion configuration and performing a simulation at a constant but high enough temperature to allow a melting of the oxygen lattice, thus equilibrating the system. The procedure is then repeated in the opposite way to enable the formation of an oxygen
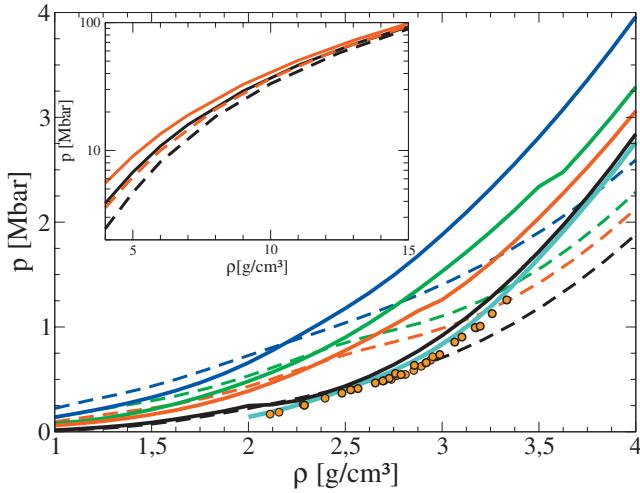
FIG. 1. (Color) QMD pressure isotherms (solid lines) in comparison with the SESAME 7150 EOS (Ref. 26) (dashed lines) for temperatures of 1000 K (black), 4000 K (red), 6000 K (green), and 10000 K (blue). The cyan line is a 300 K QMD isotherm to compare with DAC measurements of Sugimura *et al.* (Ref. 27) represented by the dots. The inset shows the 8000 K (black) and 24000 K (red) isotherms for higher densities.

lattice again from a fluid configuration. This method requires very long simulation times of up to 20 ps in each direction, but soundly narrows down the width of the phase boundary. To get converged EOS data away from the phase boundary, shorter simulation times of 0.5–2 ps, depending on density and temperature, are sufficient.

III. EQUATION OF STATE AND PHASE DIAGRAM

A. Equation of state data

In Fig. 1, we compare the QMD pressure isotherms with the SESAME 7150 EOS.[26] The QMD isotherms have a steeper slope with the density than the SESAME 7150 curves. While the QMD pressures are lower than SESAME at about 1 g/cm³, they exceed the SESAME pressures by a factor of 1.5 at 4 g/cm³. At even higher densities, this difference decreases again and both pressure curves approach each other. For instance, the deviation is less than 5% at 15 g/cm³. Sugimura *et al.*,[27] and also other groups before, have measured the thermal EOS along the 300 K (ice VII/X) isotherm up to pressures of 1.26 Mbar using diamond anvil cells. The QMD 300 K isotherm agrees within 6% or better with the measurements of Sugimura *et al.*[27] while the experimental 300 K isotherm intersects with the 1000 K SESAME isotherm at 2.8 g/cm³.

The caloric QMD EOS predicts significantly higher energies than the SESAME 7150 EOS at high densities when normalizing both EOS tables to each other at low temperatures and densities. The thermal and caloric EOS data are tabulated in Appendix E.

B. Principal Hugoniot curve

To probe water under extreme conditions experimentally, many shock-wave experiments have been performed. We
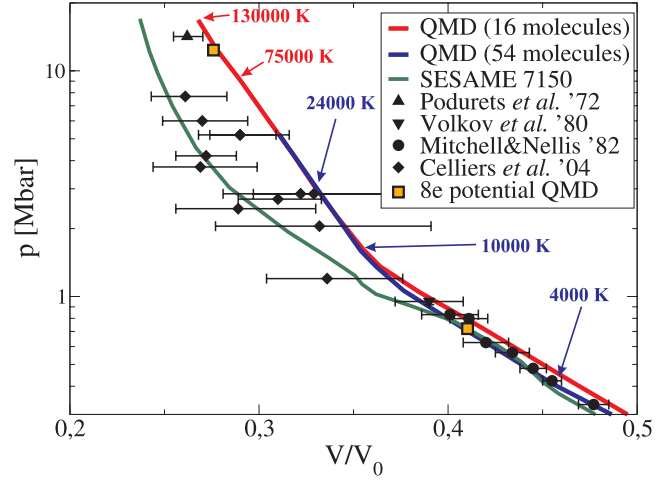

FIG. 2. (Color) Principal Hugoniot curves based on the QMD simulations in comparison with the SESAME 7150 predictions and experiments of Mitchell and Nellis (Ref. 28), Volkov *et al.* (Ref. 29), Celliers *et al.* (Ref. 30) and Podurets *et al.* (Ref. 31). Orange squares are calculations with the 8e-potential. At high temperatures, the system is a disordered plasma, reducing the need for large simulation cells: the results for 16 and 54 molecules converge.

calculate the principal Hugoniot curve via the equation $2(u-u_0)=(p+p_0)(v_0-v)$, which relates all possible final thermodynamic states generated by a planar shock waves to the initial (subscript 0) thermodynamic state. The thermodynamic variables are the specific internal energies u and u_0, the pressures p and p_0, and the specific volumes v and v_0. The principal Hugoniot uses water at ambient conditions ($T_0=295$ K, $p_0=1$ bar, $v_0^{-1}=\varrho_0=0.998$ g/cm³, specific internal energy $u_0=-77.98$ kJ/g acquired via the QMD simulations) as initial state. In Fig. 2, we present the calculated Hugoniot curve and compare with available experiments and the curve based on the SESAME 7150 EOS.[26] For weak
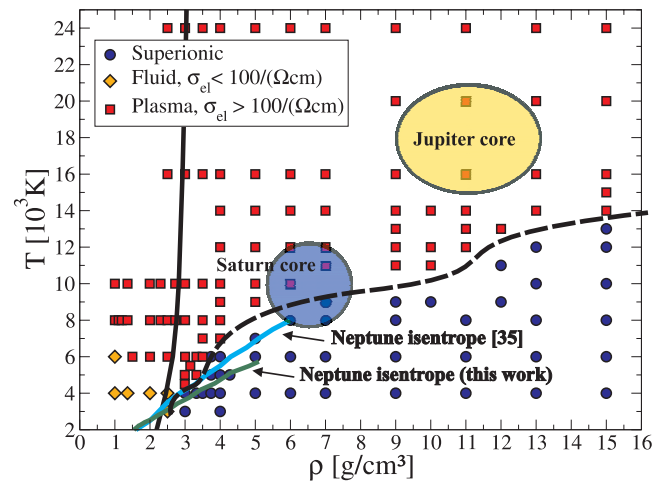

FIG. 3. (Color) Phase diagram of warm and ultradense water for temperatures above 3000 K. Each colored point represents a QMD simulation in equilibrium. The plasma-to-superionic phase boundary (black dashed line), the principal Hugoniot curve (black solid line), and two Neptune isentropes are also shown. The electronic conductivities are taken from Ref. 6.
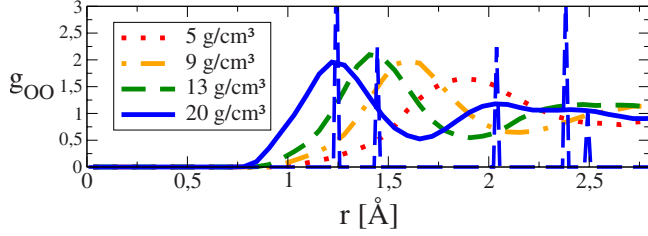
FIG. 4. (Color online) Radial oxygen-oxygen pair correlation functions at 16000 K. The picture includes also an ideal bcc lattice at 20 g/cm^3 (L_{box}=5.76 Å) to illustrate the appearance of a bcc-like short-range order already in the plasma.

shocks, both the QMD and the SESAME 7150 EOS reproduce experiments of Mitchell and Nellis[28] and Volkov *et al.*[29] very well. For very strong shocks Podurets *et al.*[31] approached nearly fourfold compression, and our results are in nice agreement with this data point, whereas SESAME 7150 predicts a higher compressibility. A deviation between both theoretical Hugoniot curves occurs in the intermediate region where Celliers *et al.*[30] recently performed laser-driven shock-wave experiments. These experiments agree with both EOS models but suggest a softer Hugoniot curve than QMD predicts, a behavior that already has been observed for deuterium.[32]

C. Phase diagram of ultradense water

We have determined the phase diagram of water from 3000 K to 24000 K and for densities up to 15 g/cm^3 which is shown in Fig. 3 (ϱ-T plane) as well as in the Appendix C (p-T-plane). The regime of the various solid high-pressure phases at lower temperatures is outside the scope of our present study. Our main result is that superionic water and

TABLE I. EOS data comparison for plane-wave cutoff energies of 900 eV and 1500 eV at the Γ point. 54 water molecules are considered in the simulation box. The absolute statistical errors are also given.

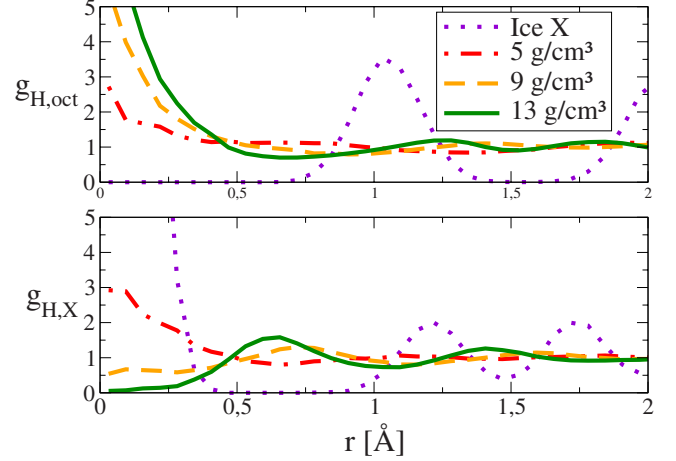| T (K)	ϱ (g/cm^3)	p_{900} (kbar)	p_{1500} (kbar)
1000	1.5	88.1 ± 0.6	88.6 ± 1.0
4000	15	88930 ± 30	88860 ± 40
6000	5	6144 ± 10	6135 ± 10
8000	2.75	1351 ± 9	1348 ± 10
24000	5	9030 ± 30	9050 ± 30
24000	15	98640 ± 50	98610 ± 40
T (K)	ϱ (g/cm^3)	u_{900} (kJ/g)	u_{1500} (kJ/g)
1000	1.5	−74.01 ± 0.03	−74.04 ± 0.06
4000	15	304.00 ± 0.12	303.88 ± 0.13
6000	5	−12.22 ± 0.11	−12.22 ± 0.13
8000	2.75	−34.76 ± 0.23	−34.8 ± 0.4
24000	5	62.2 ± 0.5	62.2 ± 0.5
24000	15	396.5 ± 0.5	396.7 ± 0.5

FIG. 5. (Color online) Protonic pair correlation functions with octahedral sites $g_{H,oct}$ and ice X positions $g_{H,X}$ in the bcc oxygen lattice at 6000 K. For comparison, we plot the same correlation functions of ice X at 4 g/cm^3 and 1000 K (dotted lines). Only the symmetric positions are occupied in ice X.

strongly dissociated fluid water are the only occurring phases above 4000 K. Dissociation is inferred from the systematic difference between the diffusion coefficients of both ion species. The coexistence line of the plasma-to-superionic phase transition is bending and shows changes in the curvature at 3.5 and at about 11 g/cm^3. The bend at 3.5 g/cm^3 is related to the ionization in the dissociated fluid above 4000 K.[6] We attribute the change of curvature at 11 g/cm^3 to a change in the proton order within the superionic phase which will be discussed in Sec. V. Because of the finite particle number in the QMD simulations, the plasma-to-superionic phase boundary can only be narrowed down to a zone. However, extrapolating the internal energies over the phase boundary along isochores, we find convincing evidence for a first-order phase transition; see Appendix C.

IV. CONSEQUENCES FOR THE GIANT PLANETS

In Fig. 3, the ovals embrace the range of conditions in the cores of Jupiter and Saturn as predicted by different planetary models.[12–15,33] We find that water at present Jupiter core conditions is in a fluid dense plasma phase, regardless of the planetary model. Hence, the initial Jupiter core may have been larger than today due to erosion of its water component. However, the Saturn core conditions are very close

TABLE II. Ground state energy ([u]=eV/molecule) of Ice X at ϱ=4 g/cm^3 for supercell sizes containing 2, 16, 54 or 128 molecules. A plane-wave cutoff of 900 eV was used.

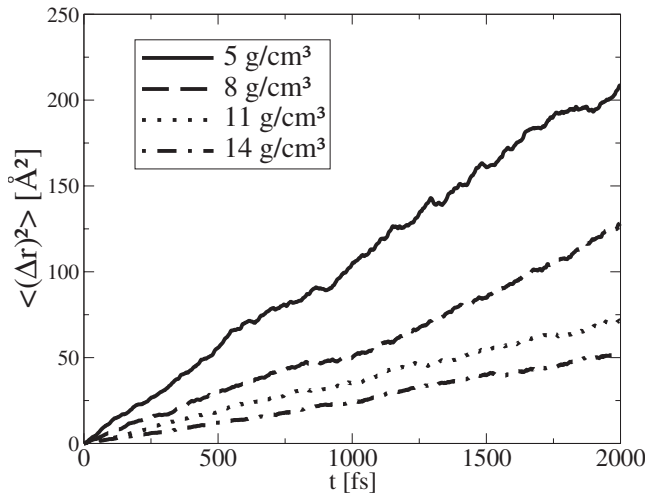| **k** points	u_2	u_{16}	u_{54}	u_{128}
Γ	−2.144	−10.565	−10.960	−10.977
$2 \times 2 \times 2$	−11.278	−10.979	−10.978	−10.978
$3 \times 3 \times 3$	−10.959	−10.978	−10.978	−10.978
$4 \times 4 \times 4$	−10.978	−10.978	−10.978	−10.978

FIG. 6. Mean square displacements for protons in superionic water at 6000 K. The simulation box contained 54 molecules.

FIG. 7. Mean square displacements for protons and oxygen ions in water plasma at 16000 K and 20 g/cm^3.

to the superionic phase boundary. For instance, the result of Gudkova and Zharkov[13] favors a superionic core, while other models[12,14,15] predict a fluid core. Thus, superionic water may exist in Saturn's core which offers an explanation why it is larger than that of Jupiter—as predicted by interior models of their present state.[15,34]

Giant planets are assumed to consist of several layers containing different concentrations of materials.[15] Fluid layers are usually convective (and thus isentropic) which is caused by a heat flow from the hotter interior to the surface while cores are isothermal. The superionic phase boundary intersects with the Neptune isentropes from earlier work[35] as well as with an isentrope that we present here. It was calculated using a three-layer model with QMD EOS data for water (present; taken also for methane) as well as for hydrogen and helium (for details, see Ref. 33 and Appendix D). It leads to core temperatures which are more than 20% lower than those from earlier results.[15,35] The first-order phase transition of water along the planetary isentrope may also help to justify more sophisticated planetary models of Uranus and Neptune, such as thin-shell dynamo models that have been proposed to explain their unusual magnetic field geometries.[36] Our findings are likely to spur intensive modeling on the structure and evolution of water-rich giant planets in and outside our solar system, e.g., like GJ 436b.[37,38]

V. IONIC STRUCTURE AND CORRELATIONS

In order to gain more insight into the phase transformations in ultradense water, we analyze the radial ion-ion pair correlation functions. In the superionic phase, the bcc oxygen lattice[2] was found to persist up to at least 15 g/cm^3 without any change. The protons show very little correlation among each other, but there is always a dominant first peak in the hydrogen-oxygen pair correlation function. This suggests strong correlations between these species which we will examine below. With increasing temperature the oxygen lattice melts but some features of the pair correlation function remain in the plasma phase. Figure 4 displays the pair
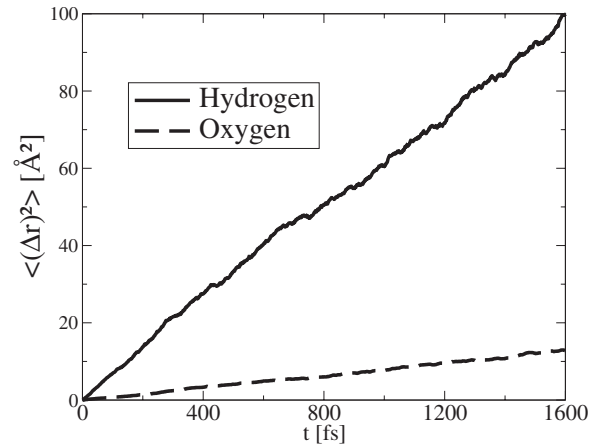
correlation functions for the fluid 16000 K isotherm up to 20 g/cm^3. A bcc-like oxygen short-range order emerges with increasing density in the fluid neighboring the superionic phase.

In the superionic phase, although the protons are highly mobile they do not move freely through the bcc oxygen lattice. Cavazzoni *et al.*[2] found that the protons prefer to jump in between the symmetric sites between two next oxygen neighbors. This is a remnant of the ice X crystal structure which becomes superionic above 2000 K. By analyzing pair correlation functions, Goldman *et al.*[3] observed the protons to occupy also off-centered positions similar to the ice VII phase, though at densities below 3 g/cm^3 and at 2000 K. Our simulations also show such a transition between both
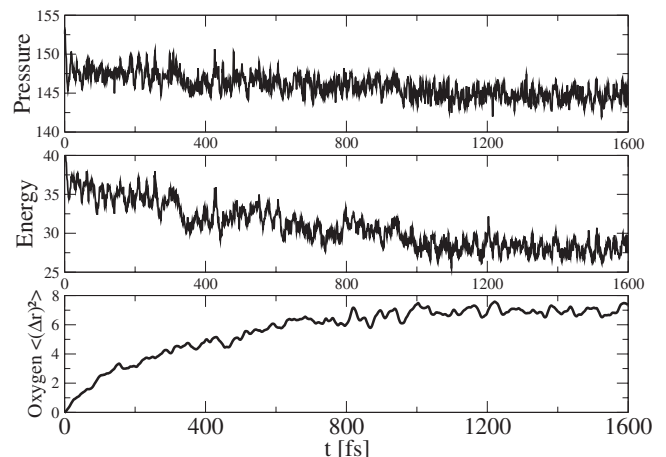
FIG. 8. Thermodynamic functions and oxygen diffusion during the formation of the superionic phase at 8000 K and 7 g/cm^3. The simulation cell contains 54 molecules and the initial configuration was a fluid at 12000 K and 7 g/cm^3. The system remains a fluid until there are simultaneous changes in energy, pressure and diffusion after 1000 fs. This particular simulation rapidly changed phase, a sign that 8000 K is deep in the superionic phase. Other points required several tens of ps long simulations before the phase transitions were observed. In the majority of our calculations the temperature difference between the initial configurations and the simulations was 2000 K.

TABLE III. Comparison of EOS data for different system sizes (*N*: number of water molecules) and **k**-point samplings. A 900 eV plane-wave energy cutoff was used in all calculations. The absolute statistical errors are also given.

T (K)	ϱ (g/cm^3)	N	**k**-points	p (kbar)	u (kJ/g)
1000	1.5	54	Γ	88.1 ± 0.6	-74.01 ± 0.03
1000	1.5	54	$2 \times 2 \times 2$	87.4 ± 0.6	-74.01 ± 0.03
1000	1.5	128	Γ	88.0 ± 1.0	-73.98 ± 0.03
4000	15	54	Γ	88930 ± 30	304.00 ± 0.12
4000	15	54	$2 \times 2 \times 2$	89890 ± 50	307.68 ± 0.10
4000	15	54	$3 \times 3 \times 3$	89950 ± 30	307.81 ± 0.10
4000	15	128	Γ	89560 ± 30	303.50 ± 0.17
4000	15	128	$2 \times 2 \times 2$	89800 ± 30	304.66 ± 0.10
6000	5	54	Γ	6144 ± 10	-12.22 ± 0.11
6000	5	54	$2 \times 2 \times 2$	6178 ± 9	-11.90 ± 0.12
6000	5	54	$3 \times 3 \times 3$	6178 ± 9	-11.88 ± 0.11
6000	5	128	Γ	6174 ± 8	-11.74 ± 0.07
8000	2.75	54	Γ	1351 ± 9	-34.76 ± 0.23
8000	2.75	54	$2 \times 2 \times 2$	1350 ± 10	-35.0 ± 0.5
8000	2.75	128	Γ	1345 ± 6	-34.69 ± 0.20
24000	5	54	Γ	9030 ± 30	62.2 ± 0.5
24000	5	54	$2 \times 2 \times 2$	9055 ± 25	62.6 ± 0.5
24000	5	128	Γ	9080 ± 30	63.0 ± 0.5
24000	15	54	Γ	98640 ± 50	396.5 ± 0.5
24000	15	54	$2 \times 2 \times 2$	98850 ± 50	397.5 ± 0.5
24000	15	54	$3 \times 3 \times 3$	98830 ± 50	397.9 ± 0.4
24000	15	128	Γ	98810 ± 40	397.9 ± 0.4
100000	3.5	16	Γ	11960 ± 60	369.6 ± 1.0
100000	3.5	27	Γ	11990 ± 70	369.0 ± 1.2
100000	4	16	Γ	14450 ± 60	373.2 ± 0.9
100000	4	16	$2 \times 2 \times 2$	14390 ± 60	372.1 ± 0.9

proton structures at 4000 and 6000 K between 4 and 5 g/cm^3. Furthermore, protons can be located at octahedral sites in the bcc oxygen lattice. Since both the symmetric and octahedral sites have similar nearest oxygen distances, we compute special pair correlation functions between the protons and both the octahedral sites $g_{H,oct}$ and with the symmetric (ice X) positions between the nearest oxygen neighbors $g_{H,X}$ which are shown in Fig. 5.

Below 5 g/cm^3, the protons are mainly found close to the symmetric sites, while passing the octahedral sites less frequently. With increasing density, they tend to avoid successively the symmetric positions and instead occupy the octahedral sites. Above 13 g/cm^3, protons are no longer found at the symmetric positions and only the octahedral sites are occupied. The protons on octahedral sites have larger distances to the nearest oxygens compared to the symmetric positions, so that this rearrangement likely stabilizes the oxygen lattice in the superionic phase by weakening the repulsive forces between the ions. The change in the curvature of the melting curve around 11 g/cm^3 in the phase diagram occurs in the same density regime. The protons are strongly diffusive throughout the phase diagram shown here.

In this paper, we do not discuss the region of the phase diagram where Benoit *et al.*[5] predict an orthorhombic ice phase at high densities above 4 g/cm^3 and below 2000 K. Such a crystal structure could in principle not occur in the cubic simulation cell that is used in all our simulations. However, starting e.g., from an ice X configuration we observed a deformation of the bcc oxygen lattice but only in that particular region of the phase diagram. This supports the conclusion that if a non-bcc oxygen lattice was present in the superionic phase at densities above 4 g/cm^3 and temperatures of 4000 K or higher, an observable distortion in the oxygen lattice would have occurred. This was not the case, nor did the oxygen ions freeze into an amorphous solid when cooling the plasma.

VI. CONCLUSIONS

We have extended the known phase diagram of water to an extreme density of 15 g/cm^3 and temperatures up to 24000 K. Although superionic water and water plasma dominate the phase diagram under these conditions, we identify a gradual structural change in the proton distribution of the superionic phase and a corresponding shift in the phase boundary at high density. We have performed all-electron calculations to validate these findings and to acquire EOS

TABLE IV. Comparison of EOS data for the all-electron PAW core potential (2000 eV cutoff) with the six-electron PAW core potential (900 eV cutoff). The Γ point was used for all calculations. The internal energies are defined to be equal at the 1000 K simulation.

T (K)	ϱ (g/cm^3)	N	p_{6e} (kbar)	p_{8e} (kbar)
1000	2.0	54	246 ± 2	247 ± 2
4000	3.0	54	1259 ± 6	1266 ± 12
4000	15.0	54	88930 ± 30	88150 ± 70
6000	5.0	54	6144 ± 10	6127 ± 9
8000	7.0	54	15280 ± 15	15220 ± 15
14000	9.0	54	30140 ± 25	29970 ± 25
24000	15.0	54	98640 ± 50	97440 ± 50
100000	3.0	16	9690 ± 40	9560 ± 50
100000	3.5	16	11960 ± 60	11800 ± 50
100000	4.0	16	14450 ± 60	14400 ± 50
T (K)	ϱ (g/cm^3)	N	u_{6e} (kJ/g)	u_{8e} (kJ/g)
1000	2.0	54	-72.40 ± 0.15	$\overset{!}{=} -72.4 \pm 0.3$
4000	3.0	54	-52.37 ± 0.09	-52.31 ± 0.25
4000	15.0	54	304.00 ± 0.12	302.7 ± 0.3
6000	5.0	54	-12.22 ± 0.11	-12.19 ± 0.3
8000	7.0	54	44.88 ± 0.15	44.97 ± 0.3
14000	9.0	54	137.2 ± 0.5	136.5 ± 0.5
24000	15.0	54	396.5 ± 0.5	395.5 ± 0.7
100000	3.0	16	368.6 ± 0.7	367.7 ± 0.9
100000	3.5	16	369.6 ± 1.0	369.3 ± 1.2
100000	4.0	16	373.2 ± 1.0	374.2 ± 1.2

data and detailed structural information. The QMD simulations reproduce shock-wave experiments well while displaying significant differences to the SESAME 7150 EOS. We predict superionic water to exist in Neptune. It can probably be found also in Saturn's core but not in that of Jupiter. Our results are of great importance for planetary physics, especially for interior models of water-rich giant planets.

ACKNOWLEDGMENTS

APPENDIX A: CONVERGENCE OF THE EOS DATA

The convergence of first-principles calculations has to be studied in detail[39] since that determines and limits their qual-

TABLE V. Thermal $p(T,\varrho)$ and caloric $u(T,\varrho)$ EOS of water with 54 molecules in the simulation box. (Isotherms 1000 K, 2000 K, 3000 K, and 4000 K.)

| T (K)	ϱ (g/cm^3)	p (kbar)	u (kJ/g)
1000 (fluid)	1.0	18.6	-74.48
1000 (fluid)	1.108	28.4	-74.42
1000 (fluid)	1.246	43.5	-74.43
1000 (fluid)	1.5	88.1	-74.01
1000 (fluid)	1.75	158	-73.32
1000 (fluid)	1.9	207	-72.77
1000 (fluid)	1.994	246	-72.40
1000 (ice VII)	2.5	436	-71.29
1000 (ice VII)	3.0	918	-67.68
1000 (ice X)	3.5	1720	-62.16
1000 (ice X)	4.0	2840	-54.52
2000 (fluid)	1.0	36.8	-70.83
2000 (fluid)	1.108	49.1	-70.81
2000 (fluid)	1.151	56.3	-70.81
2000 (fluid)	1.36	87.9	-70.34
2000 (fluid)	1.5	120	-69.96
2000 (fluid)	1.76	196	-69.20
2000 (fluid)	2.0	304	-67.90
2000 (fluid)	2.301	478	-66.20
2000 (superi.)	2.5	593	-65.18
2000 (superi.)	2.75	790	-63.88
2000 (superi.)	3.0	1050	-62.78
2000 (ice X)	3.25	1400	-60.57
2000 (ice X)	3.5	1830	-57.64
2000 (ice X)	3.75	2340	-54.05
2000 (ice X)	4.0	2900	-50.24
3000	2.5	694	-60.4
3000	3.0	1180	-56.5
3000	3.5	1950	-50.5
3000	4.0	2960	-42.9
4000	0.9972	59.5	-63.3
4000	1.36	126	-62.0
4000	1.994	385	-59.4
4000	2.5	776	-55.7
4000	3.0	1260	-52.4
4000	3.324	1730	-48.7
4000	3.5	2040	-46.4
4000	4.0	3060	-38.8
4000	5.0	5870	-19.9
4000	6.0	9660	3.3
4000	7.0	14400	29.6
4000	9.0	27030	88.7
4000	11.0	44050	155.8
4000	13.0	64160	228.7
4000	15.0	88930	304.0
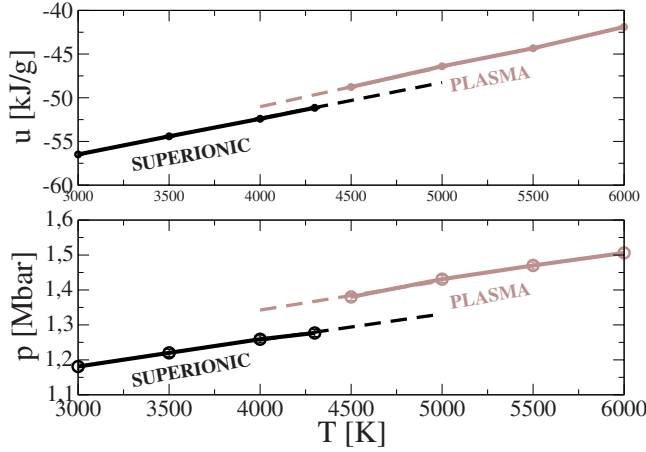
FIG. 9. (Color online) The 3 g/cm³ isochore showing discontinuities in the thermodynamic functions. For this example, the transition temperature was determined to an accuracy of 200 K. This required simulation times of 15 ps. The symbol sizes represent the statistical error of the pressure and energy, see Sec. I.

ity. We show that the accuracy of our thermal EOS is better than 2% including statistical uncertainties. No relative error can be given for the internal energy, but the results are of the same quality. In our analysis we focus on the influence of the finite system size, the number of **k** points, the cutoff energy and the validity of the pseudopotentials, which contribute to the systematic errors. The statistical errors (95% confidence interval) are calculated as well. After thermalization, the averaging of EOS data was performed with 2500 time steps for 16 molecules, 1500 time steps for 54 molecules, and 800 time steps for 128 molecules in the simulation box.

1. Cutoff energy

The simulations were performed with the standard PAW pseudopotentials provided by VASP 4.6 for hydrogen (1 free electron) and oxygen (6 free electrons). In an earlier work,[6,40] it was shown that a plane-wave cutoff energy of 900 eV was sufficient to converge the pressure to better than 2% at lower densities. It was found that the internal energy converged already using lower cutoffs. In this work, we confirm and specify those results by comparing several of our EOS data points in Table I with simulations using a 1500 eV cutoff energy. Table I shows that the deviations between the 900 eV and the 1500 eV calculations are statistically insignificant. A systematic over- or underestimation of the pressure or energy does not exist.

2. Particle number and k points

The number of **k** points and of particles are not independent quantities for convergence issues. A higher particle number leads to a smaller first Brillouin zone and, thus, decreases the influence of band dispersion. The necessary amount of **k** points can be reduced. In Table II, we show the convergence of the ground state energy for Ice X supercells containing different numbers of unit cells with respect to **k**-point sets using the method of Monkhorst and Pack.[41]
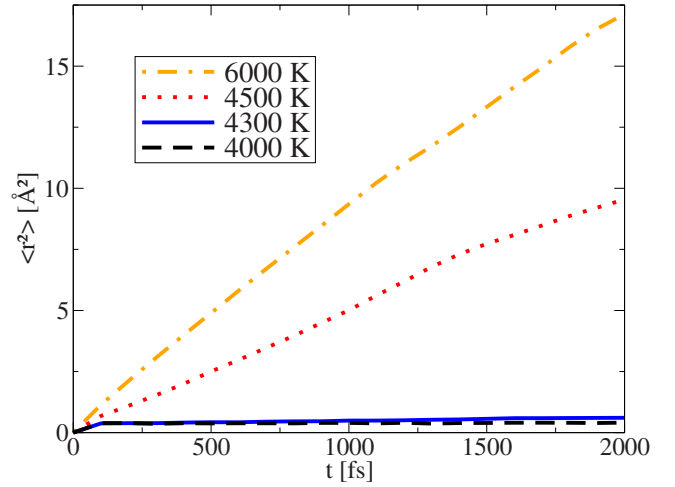

FIG. 10. (Color online) Mean square displacements for the oxygen ions at the 3 g/cm³ isochore. The oxygen movement is diffusive at 4500 K and higher temperatures. At 4300 K or lower temperatures they can only vibrate around their bcc lattice positions and, thus, show no diffusive movement.

The results show clearly that the energy converges rapidly if enough particles are considered. For a 54 molecules supercell the deviation from the Γ-point value to the converged result is less than 0.02 eV. We have also checked the convergence of our QMD simulations using both higher **k**-point and particle numbers. The results for the respective EOS data are given in the Table III. For instance, calculations with 54 molecules at the Γ-point are sufficient to get a maximum deviation of the pressure of about 1%. This occurs in the cold dense region of the phase diagram (4000 K, 15 g/cm³) where the pressure is underestimated. The deviations are smaller in regions where the temperature is higher and the
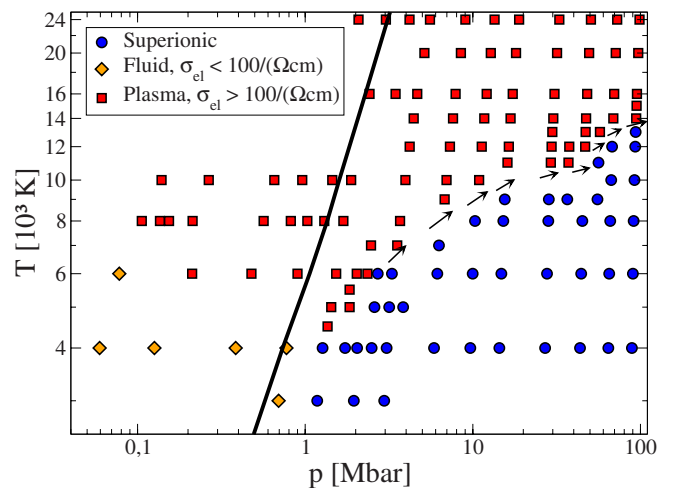

FIG. 11. (Color online) Phase diagram of warm and ultradense water for temperatures above 3000 K. Each colored point represents a QMD simulation in equilibrium. The principal Hugoniot curve (black solid line) is also shown. The electronic conductivities are taken from Ref. 6. The arrows represent the slope of the phase boundary calculated by the Clausius-Clapeyron equation above 4 g/cm³.

density lower. The internal energy converges in the same manner. For the very high temperature states on the Hugoniot curve, simulations performed with 16 molecules produced already well converged results.

3. Pseudopotentials

Our QMD calculations extend also to extreme areas of the phase diagram, i.e., densities of 15 g/cm^3 as well as temperatures up to 130000 K using the standard VASP PAW pseudopotentials. The standard oxygen pseudopotential treats only 6 of 8 electrons within the DFT algorithm. The $1s$ electrons are very strongly bound to the core ($\Delta E(O^{6+} \to O^{7+}) \approx 740$ eV). The core electrons are located, assuming a hydrogenlike atom, at a distance of $\langle 1s|r|1s \rangle = 3a_B/16 \approx 0.10$ Å.[42] In our simulations such small ion-ion distances were not observed and we do not expect the 1s electrons to be ionized. We have nevertheless performed several QMD runs with an all electron PAW core potential[24] which requires a plane-wave energy cutoff of 2000 eV, to test the validity of our calculations. We compare the results in Table IV for different thermodynamic conditions. The employment of the standard oxygen potential results in an overestimation of pressure and energy by up to 1.5% at the very high densities. The deviation does not occur at lower densities as well as for very high temperature Hugoniot states.

4. Conclusions on the EOS convergence

In conclusion, the statistical error, ranging from below 1% to 0.05% dominates at lower densities, while **k** points, higher particle numbers, and the pseudopotentials make little contributions to the error. We conclude that the QMD EOS is accurate up to 1% for the conditions relevant for the giant planet's interiors of our solar system. At higher densities and low temperatures, the evaluation at the Γ point leads to an underestimation of pressure and energy while the use of the standard oxygen potential causes an overestimation of the EOS. This leads to an overall error of up to 2% for the entire QMD EOS.

APPENDIX B: DIFFUSION COEFFICIENTS

We use the self-diffusion coefficients in order to identify different phases in the phase diagram. After thermodynamic equilibrium, the mean square displacement is recorded for both ion species and the self-diffusion coefficient is obtained. Depending on the location in the phase diagram, we either observed a diffusive behavior ($\langle r^2 \rangle \sim t$, see Fig. 6) or no movement ($\langle r^2 \rangle$=const., e.g., oxygen ions in the superionic phase).

The proton self-diffusion coefficient behaves systematically in the whole phase diagram. It increases with the temperature but decreases with the density. The plasma-to-superionic phase transition yields no abrupt changes of the proton self-diffusion coefficients. In the plasma phase, the oxygen mean square displacement behaves linearly even when the pair correlation functions depict similarities to a bcc lattice, as, e.g., at 16000K and 20 g/cc, see Fig. 4 and Fig. 7.

TABLE VI. Thermal $p(T, \varrho)$ and caloric $u(T, \varrho)$ EOS of water with 54 molecules in the simulation box. (Isotherms 6000 K, 8000 K, 9000 K, and 10000 K.)

T (K)	ϱ (g/cm^3)	p (kbar)	u (kJ/g)
6000	0.9972	77.7	−52.5
6000	1.5	212	−51.6
6000	1.994	478	−49.6
6000	2.5	901	−45.9
6000	3.0	1530	−41.5
6000	3.324	2030	−38.0
6000	3.5	2340	−36.1
6000	3.739	2710	−34.7
6000	4.0	3290	−30.9
6000	5.0	6140	−12.2
6000	6.0	9980	10.8
6000	7.0	14850	37.4
6000	9.0	27670	97.0
6000	11.0	44790	164.3
6000	13.0	65160	237.6
6000	15.0	90140	313.3
8000	1.0	108	−41.3
8000	1.36	213	−42.1
8000	1.994	565	−40.1
8000	2.301	821	−38.5
8000	2.5	1030	−37.2
8000	2.719	1300	−35.1
8000	2.75	1350	−34.8
8000	2.992	1690	−32.4
8000	3.5	2590	26.2
8000	4.0	3680	−18.9
8000	6.0	10300	18.6
8000	7.0	15270	44.9
8000	9.0	28260	104.8
8000	11.0	45510	172.7
8000	13.0	66000	246.1
8000	15.0	91170	321.9
9000	4.0	3820	−14.3
9000	5.0	6790	4.7
9000	7.0	15480	48.8
9000	9.0	28540	109.0
9000	10.0	36620	142.0
9000	12.0	55390	213.3
10000	0.9972	139	−32.1
10000	1.36	266	−33.6
10000	1.994	654	−31.9
10000	2.301	960	−30.5
10000	2.719	1450	−27.4
10000	3.0	1880	−23.9
10000	3.5	2810	−17.4
10000	4.0	3960	−9.7
10000	5.0	6970	9.4

TABLE VI. (*Continued.*)

T (K)	ϱ (g/cm^3)	p (kbar)	u (kJ/g)
10000	6.0	10920	31.6
10000	13.0	66850	254.0
10000	15.0	92150	330.1

APPENDIX C: PLASMA-TO-SUPERIONIC PHASE TRANSITION

The boundaries of the phase transition were located by performing QMD simulations at constant densities. Starting with a fluid ion configuration, the temperature is lowered and equilibration reached at the new temperature. The movement of the ions is followed, but the structure is more importantly determined when the system has reached equilibrium: either the system remains fluid or a bcc lattice is formed. If a bcc lattice is formed, the new temperature constitutes a lower bound for the metastability of the supercooled fluid. The same protocol is followed to locate the upper bound of the phase transition. An initial superionic configuration is used and the temperature increased; but kept constant over the simulation. If the oxygen lattice melts, the new temperature is an upper bound for the stability of the superionic phase. In the phase diagram (Figs. 3 and 11), this applies for all color coded points close to the phase boundary: blue means that a fluid structure turned superionic while a red point means that a superionic structure turned fluid. The points thus represent the boundaries of the phase transition. The methodology closely resembles the technique of ramping the temperature in an isochoric simulation.

Figure 8 shows a typical example of the converging pressure, internal energy, and oxygen diffusion. The bcc oxygen lattice can be identified by computing a pair correlation function with time-averaged oxygen positions. No amorphous phase has been observed.

The location of the phase boundary can only be determined with finite accuracy. To identify the order of the phase transition, we plot the specific internal energy as well as the pressure versus the temperature along isochores crossing the phase boundary, see Fig. 9. For the displayed isochore, the oxygen movement is plotted in Fig. 10, respectively. When extrapolating the EOS across the phase boundary, we find strong evidence for a discontinuity and hence a first-order phase transition. Since the transition from superionic to fluid involves the melting of the oxygen lattice, it is not surprising that the phase transition is first order. On the contrary, given the large increase in entropy between a lattice structure and a fluid, a second order transition is unlikely. The respective heat of transition can be estimated.

In Fig. 11 the phase diagram is presented in the pressure vs temperature plane. At about 3.5 g/cm^3 (2 Mbar) the phase boundary shows a change in the curvature. Such a bending of the phase boundary is caused by changes of the thermodynamic variables in at least one of the phases which have its origin in the changes of the microscopic properties of the system. The ionization process and, thus, the increase in the electronic entropy that occurs in the fluid at about

TABLE VII. Thermal $p(T,\varrho)$ and caloric $u(T,\varrho)$ EOS of water with 54 molecules in the simulation box. (Isotherms 11000 K, 12000 K, 13000 K, 14000 K, 16000 K, 20000 K, and 24000 K.)

T (K)	ϱ (g/cm^3)	p (kbar)	u (kJ/g)
11000	7.0	16170	63.1
11000	9.0	29230	122.6
11000	12.0	56160	221.4
12000	4.0	4200	−1.9
12000	5.0	7300	18.3
12000	6.0	11320	40.7
12000	7.0	16370	67.1
12000	9.0	29520	127.5
12000	10.0	37640	160.7
12000	13.0	67680	262.4
12000	15.0	93110	338.5
13000	9.0	29820	132.0
13000	11.0	47110	200.2
13000	12.0	57290	236.2
13000	15.0	93590	342.6
14000	4.0	4440	5.9
14000	5.0	7620	26.3
14000	6.0	11750	50.0
14000	7.0	16830	76.0
14000	9.0	30140	137.2
14000	10.0	38310	170.8
14000	11.0	47500	205.8
14000	13.0	68860	278.4
14000	15.0	94340	354.6
16000	4.0	4660	12.9
16000	5.0	7900	33.5
16000	6.0	12110	57.7
16000	7.0	17280	84.4
16000	9.0	30720	145.9
16000	11.0	48190	214.0
16000	13.0	69660	287.0
16000	15.0	95260	364.0
20000	4.0	5140	27.8
20000	5.0	8490	48.2
20000	6.0	12810	72.6
20000	7.0	18120	100.0
20000	9.0	31820	161.8
20000	11.0	49470	230.4
20000	13.0	71180	303.6
20000	15.0	96980	381.4
24000	4.0	5550	41.2
24000	5.0	9030	62.2
24000	6.0	13470	86.9
24000	7.0	18890	114.3
24000	9.0	32790	177.2
24000	11.0	50650	245.0
24000	13.0	72610	319.9

TABLE VII. (*Continued.*)

T (K)	ϱ (g/cm^3)	p (kbar)	u (kJ/g)
24000	15.0	98710	397.1

4000 K, is responsible for the this bending; see Ref. 6 for detailed conductivity calculations in this region. A second change in the curvature between 10 and 12 g/cm^3 occurs just when the protons cease to move through the symmetric sites and only pass through the octahedral sites. This does not affect the entropy differences Δs much but has more drastic consequences on the volume differences Δv of both phases. Evaluating the Clausius-Clapeyron equation $dT/dp = \Delta v/\Delta s$, we can estimate the slope of the phase boundary for each isobar. The slope behaves systematically but there is a noticeable increase between 11 and 12 g/cm^3 (about 55 Mbar) by a factor of 2. This result illustrates the trends for the slope which are in qualitative agreement with the phase boundary directly acquired from the QMD simulations. The errors of Δv and Δs are 10%–20% each, which does not allow for an accurate integration of the Clausius-Clapeyron equation. Although a first-order phase transition occurs, the differences Δv and Δs are small quantities which means that both phases behave thermodynamically very similarly. This is not surprising since only every third ion (the oxygen ions) is involved in the melting of the superionic oxygen lattice, a structure already significantly softened due to thermal motion.

APPENDIX D: DETAILS ON THE CALCULATION THE NEPTUNE ISENTROPE

The Neptune isentrope (see Fig. 3 in the paper) shows the density of water along the adiabatic temperature profile of an interior model of Neptune. An underlying assumption of this model is a three-layer structure with an isothermal core of rocks and two isentropic envelopes composed of hydrogen, helium and water. The transition pressure between the envelopes is set to 21 GPa at 2150 K in accordance with the transition to high protonic conductivity.[6] The water mass fractions of 40% in the outer and 92% in the inner envelope are fixed by the constraints to match the observed gravitational moments J_2 and J_4. Further observables[15] considered and reproduced by this model are the total mass, the aequatorial radius, the surface temperature, the period of rotation,

TABLE VIII. Thermal $p(T,\varrho)$ and caloric $u(T,\varrho)$ EOS of water with 27 or 16 molecules in the simulation box for densities below 1 g/cm^3.

T (K)	ϱ (g/cm^3)	p (kbar)	u (eV/atom)
1000	0.3739	0.709	−4.594
1000	0.4986	1.325	−4.609
1000	0.7479	6.032	−4.628
2000	0.3739	4.673	−4.413
2000	0.4986	6.784	−4.415
2000	0.5983	8.853	−4.389
2000	0.7479	15.43	−4.407
4000	0.3739	10.48	−4.044
6000	0.3739	17.35	−3.424
8000	0.2493	13.94	−2.376
8000	0.3739	22.4	−2.338
8000	0.4986	31.06	−2.486
8000	0.7479	58.79	−2.446
10000	0.1108	9.81	−1.486
10000	0.2493	20.45	−1.548
10000	0.3739	33.02	−1.855
10000	0.4986	44.42	−1.734
10000	0.7479	79.49	−1.937

and the helium abundance (27%). According to this model, superionic water contributes about 55% to Neptune's total mass; see[33] for more detailed information on the modeling procedure.

APPENDIX E: TABULATED EOS DATA

We present the water EOS data in Tables V–VII. All simulations were performed with 54 molecules, the standard VASP PAW potentials with a 900 eV plane-wave cutoff and evaluation of the electronic states at the Γ point. The thermodynamic phase information is also given for the 1000 and 2000 K isotherms which are not displayed in the phase diagrams. Mattsson and Desjarlais[6] have decided to include additional EOS data from their work for densities below 1 g/cm^3 in this supplement, see Table VIII. These data were obtained using the same simulation parameters except that 16 or 27 molecules were in the simulation box. Some of these data were published in Ref. 43 but not in tabular form.

[1] V. F. Petrenko and R. W. Whitworth, *Physics of Ice* (Oxford University Press, Oxford, 1999).

[2] C. Cavazzoni, G. L. Chiarotti, S. Scandolo, E. Tosatti, M. Bernasconi, and M. Parrinello, Science **283**, 44 (1999).

[3] N. Goldman, L. E. Fried, I-Feng W. Kuo, and C. J. Mundy, Phys. Rev. Lett. **94**, 217801 (2005).

[4] A. F. Goncharov, N. Goldman, L. E. Fried, J. C. Crowhurst, I-Feng W. Kuo, C. J. Mundy, and J. M. Zaug, Phys. Rev. Lett.

94, 125508 (2005).

[5] M. Benoit, M. Bernasconi, P. Focher, and M. Parrinello, Phys. Rev. Lett. **76**, 2934 (1996).

[6] T. R. Mattsson and M. P. Desjarlais, Phys. Rev. Lett. **97**, 017801 (2006).

[7] V. N. Zharkov and V. P. Trubitsyn, *Physics of Planetary Interiors*, edited by W. B. Hubbard (Parchart, Tucson, 1978).

[8] W. B. Hubbard, Science **214**, 145 (1981).

⁹ W. B. Hubbard and M. S. Marley, Icarus **78**, 102 (1989).

¹⁰ J. B. Pollack, O. Hubickyj, P. Bodenheimer, J. J. Lissauer, M. Podolak, and Y. Greenzweig, Icarus **124**, 62 (1996).

¹¹ T. Guillot, Science **286**, 72 (1999).

¹² G. Chabrier, D. Saumon, W. B. Hubbard, and J. I. Lunine, Astrophys. J. **391**, 817 (1992).

¹³ T. V. Gudkova and V. N. Zharkov, Planet. Space Sci. **47**, 1201 (1999).

¹⁴ G. I. Kerley, *Kerley Technical Services KTS04–1* (Appomattox, 2004).

¹⁵ T. Guillot, Annu. Rev. Earth Planet. Sci. **33**, 493 (2005).

¹⁶ I. Baraffe, G. Chabrier, and T. Barman, Astron. Astrophys. **482**, 315 (2008).

¹⁷ M. J. Gillan, D. Alfè, J. Brodholt, L. Vočadlo, and G. D. Price, Rep. Prog. Phys. **69**, 2365 (2006).

¹⁸ G. Kresse and J. Hafner, Phys. Rev. B **47**, 558 (1993); **49**, 14251 (1994); G. Kresse and J. Furthmüller, *ibid.* **54**, 11169 (1996).

¹⁹ P. Hohenberg and W. Kohn, Phys. Rev. **136**, B864 (1964).

²⁰ W. Kohn and L. J. Sham, Phys. Rev. **140**, A1133 (1965).

²¹ N. D. Mermin, Phys. Rev. **137**, A1441 (1965).

²² J. P. Perdew, K. Burke, and M. Ernzerhof, Phys. Rev. Lett. **77**, 3865 (1996).

²³ P. E. Blöchl, Phys. Rev. B **50**, 17953 (1994); G. Kresse and D. Joubert, *ibid.* **59**, 1758 (1999).

²⁴ G. Kresse (private communication).

²⁵ S. Nosé, J. Chem. Phys. **81**, 511 (1984).

²⁶ S. P. Lyon and J. D. Johnson, Los Alamos Report No. LA-UR-92–3407, 1992. SESAME 7150 was developed before 1980 and is not considered a state-of-the-art EOS. However, it is widely available and still considered an important benchmark.

²⁷ E. Sugimura, T. Iitaka, K. Hirose, K. Kawamura, N. Sata, and Y. Ohishi, Phys. Rev. B **77**, 214103 (2008).

²⁸ A. C. Mitchell and W. J. Nellis, J. Chem. Phys. **76**, 6273 (1982).

²⁹ L. P. Volkov, N. P. Voloshin, R. A. Mangasarov, V. A. Simonenko, G. V. Sin'ko, and V. L. Sorokin, JETP Lett. **31**, 513 (1980).

³⁰ P. M. Celliers, G. W. Collins, D. G. Hicks, M. Koenig, E. Henry, A. Benuzzi-Mounaix, D. Batani, D. K. Bradley, L. B. Da Silva, R. J. Wallace, S. J. Moon, J. H. Eggert, K. K. M. Lee, L. R. Benedetti, R. Jeanloz, I. Masclet, N. Dague, B. Marchet, M. Rabec Le Gloahec, C. Reverdin, J. Pasley, O. Willi, D. Neely, and C. Danson, Phys. Plasmas **11**, L41 (2004).

³¹ M. A. Podurets, G. V. Simakov, R. F. Trunin, L. V. Popov, and B. N. Moiseev, Sov. Phys. JETP **35**, 375 (1972).

³² W. J. Nellis, Rep. Prog. Phys. **69**, 1479 (2006).

³³ N. Nettelmann, B. Holst, A. Kietzmann, M. French, R. Redmer, and D. Blaschke, Astrophys. J. **683**, 1217 (2008).

³⁴ M. Podolak, Science **317**, 1330 (2007).

³⁵ W. B. Hubbard, M. Podolak, and D. J. Stevenson, *Neptune and Triton* (University of Arizona Press, Tucson, AZ, 1995).

³⁶ S. Stanley and J. Bloxham, Nature (London) **428**, 151 (2004).

³⁷ R. P. Butler, S. S. Vogt, G. W. Marcy, D. A. Fischer, J. T. Wright, G. W. Henry, G. Laughlin, and J. J. Lissauer, Astrophys. J. **617**, 580 (2004).

³⁸ H. L. Maness, G. W. Marcy, E. B. Ford, P. H. Hauschildt, A. T. Shreve, G. B. Basri, R. P. Butler, and S. S. Vogt, Publ. Astron. Soc. Pac. **119**, 90 (2007).

³⁹ A. E. Mattsson, P. A. Schultz, M. P. Desjarlais, T. R. Mattsson, and K. Leung, Modell. Simul. Mater. Sci. Eng. **13**, R1 (2005).

⁴⁰ T. R. Mattsson and M. P. Desjarlais, EPAPS Document No. E-PRLTAO-97-036628.

⁴¹ H. J. Monkhorst and J. D. Pack, Phys. Rev. B **13**, 5188 (1976).

⁴² F. Schwabl, *Quantenmechanik* (Springer-Verlag, Berlin, 1998).

⁴³ T. R. Mattsson and M. P. Desjarlais, Sandia National Laboratories Report No. SAND2006–7539, 2007 (unpublished).